



The influence of multiscale heterogeneity on recrystallization in nickel processed by accumulative roll bonding

Mishin, Oleg; Zhang, Yubin; Godfrey, A.

Published in:
Journal of Materials Science

Link to article, DOI:
[10.1007/s10853-016-0566-4](https://doi.org/10.1007/s10853-016-0566-4)

Publication date:
2017

Document Version
Peer reviewed version

[Link back to DTU Orbit](#)

Citation (APA):

Mishin, O., Zhang, Y., & Godfrey, A. (2017). The influence of multiscale heterogeneity on recrystallization in nickel processed by accumulative roll bonding. *Journal of Materials Science*, 52(5), 2730-2745. DOI: 10.1007/s10853-016-0566-4

DTU Library

Technical Information Center of Denmark

General rights

Copyright and moral rights for the publications made accessible in the public portal are retained by the authors and/or other copyright owners and it is a condition of accessing publications that users recognise and abide by the legal requirements associated with these rights.

- Users may download and print one copy of any publication from the public portal for the purpose of private study or research.
- You may not further distribute the material or use it for any profit-making activity or commercial gain
- You may freely distribute the URL identifying the publication in the public portal

If you believe that this document breaches copyright please contact us providing details, and we will remove access to the work immediately and investigate your claim.

The influence of multiscale heterogeneity on recrystallization in nickel processed by accumulative roll bonding

O. V. Mishin^{1,*} • Y. B. Zhang¹ • A. Godfrey²

¹ Section for Materials Science and Advanced Characterization, Department of Wind Energy, Technical University of Denmark, Risø Campus, 4000 Roskilde, Denmark

² Key Laboratory of Advanced Materials (MOE), School of Materials Science and Engineering, Tsinghua University, Beijing 100084, China

Keywords: accumulative roll bonding, deformation structure, heterogeneity, nickel, recrystallization

Abstract: Microscopic and sample-scale heterogeneities have been characterized in nickel processed by accumulative roll bonding to a von Mises strain of 4.8, and their influence on recrystallization has been analyzed. The microscopic heterogeneities in this material are mostly associated with regions near the bonding interface, which are more refined and thus possess a higher stored energy than other regions. These regions also contain characteristic particle deformation zones around fragments of the steel wire brush used to prepare the surface for bonding. The sample-scale heterogeneities are seen as variations in the distribution of different texture components and in the fractions of high misorientation regions between the subsurface, intermediate and center layers. Each of these heterogeneities affects the progress of recrystallization. Regions near bonding interfaces, particle deformation zones and shear bands are all found to act as preferential nucleation sites. On the sample scale, recrystallization proceeds faster in the intermediate layer than in the center and subsurface layers. Comparing the progress of recrystallization in ARB-processed nickel and conventionally rolled nickel, it is evident that

* Corresponding author: e-mail: olmi@dtu.dk

additional deformation heterogeneities induced by ARB result in nucleation taking place over a more extended period of time.

Introduction

Accumulative roll bonding (ARB) is a comparatively simple deformation process which allows very high strains to be achieved by a repetitive cycle consisting typically of 50 % rolling, cutting of the rolled material in half, cleaning and wire brushing of the surface, and stacking the halves to be rolled again in subsequent cycles [1,2]. It has been shown that ARB to high strains results in significant structural refinement and large fractions of high angle boundaries (HABs). For example, the average boundary spacing measured along the normal direction (ND) in ARB-processed nickel after a von Mises strain ε_{vM} of 6.4 is $\sim 0.1 \mu\text{m}$ and the fraction of HABs is $\sim 60\%$ [3]. There are, however, significant through-thickness heterogeneities both in texture [4–10] and in the deformed microstructure [9–14] after ARB. The latter has been observed both at the microscopic scale and at the sample scale. At the microscopic scale, microstructural heterogeneities are present within each individual bonding layer in the form of atypically fine subgrains found in the near-interface regions [10–14] and coarse particles present only along the bonding interface [14–17]. At the sample scale, microstructural heterogeneities have been described in terms of high misorientation regions (HMRs) and low misorientation regions (LMRs) found in different proportions in subsurface, intermediate and center layers of the ARB stack [9].

Sample-scale heterogeneities in deformed microstructures are known to affect the recrystallization behavior, including both nucleation [18–20] and growth kinetics [21]. However, very little work has been done to investigate the influence of multiscale heterogeneities induced by ARB on recrystallization. Only microscopic heterogeneities related to the bonding interfaces have been

considered in annealed ARB samples of copper [22] and aluminum [23], where the final grain size was found to be smaller near the interfaces than in the center of the bonded layers. The origin of the coarse particles seen along the interfaces and their effect on nucleation have not been studied in these publications.

In this work, the influence of both microstructural and sample-scale heterogeneities on the recrystallization behavior is investigated using an ARB-processed nickel sample that has previously been shown to contain both microscopic and sample-scale heterogeneities after deformation [9]. Several questions are addressed in this study, namely: (i) how do the microscopic heterogeneities induced by ARB affect the spatial distribution of nucleation sites?; (ii) how do the sample-scale heterogeneities affect the final grain size and recrystallization texture?; and (iii) how do all these heterogeneities affect the overall recrystallization kinetics, nucleation and growth rates? To our knowledge, the present work is the first where the recrystallization process is analyzed ~~based on~~ by combining both a microscopic and sample-scale characterization of an ARB-processed material. To evaluate how the recrystallization behavior after ARB differs from that after conventional rolling, the results obtained in the present work are compared to the literature data for rolled nickel.

Experimental

A pure (99.967 %) nickel sample with an initial grain size of approximately 20 μm , processed by ARB to a von Mises strain $\varepsilon_{\text{vM}} = 4.8$ [9], was used in the present work. For this sample, the first 50 % rolling pass was conducted on a strip with an initial thickness of 2 mm, while stacking and bonding cycles started from the second pass. Lubrication was used for each rolling pass. To enable good bonding during rolling, the strip surface was cleaned with acetone and treated with a steel wire brush. In total, 6 rolling passes (i.e. 5 bonding cycles) were used, resulting in a sample containing 32 individual ARB layers. This material was annealed in air at 220 °C for different periods of time. For microstructural

investigations, the longitudinal section, which contained the rolling direction (RD) and the normal direction (ND), was inspected in a Zeiss Supra 35 scanning electron microscope using X-ray energy dispersive spectrometry (EDS), BSE imaging and the EBSD technique.

A step size of 50 nm was used for studying the deformed and recovered microstructure by EBSD. A larger step size of 0.5 μm was used for analysis of recrystallization and texture, for which a total area of at least 1 mm^2 was mapped covering the entire thickness of the sample. Since considerable differences in the microstructure and texture were observed in the deformed sample between subsurface, intermediate and central layers [9], these layers were analyzed separately in the present work also for the annealed samples. Each of these layers was defined as 1/5 of the sample thickness (see Fig. 1). For the subsurface and intermediate layers, the data obtained in the top and bottom sides of the ARB sample were averaged.

Except for regions containing coarse particles, the EBSD indexing fraction was at least 72 % for the deformed microstructure, and increased with increasing annealing duration to 90 % after 210 min of annealing. Non-indexed points in the data were filled with orientations of neighboring points using the noise-reduction filter in the post-processing software. The filtering was controlled so as to be sufficient to reassign orientations to non-indexed points along grain boundaries and sub-boundaries, while ensuring that clusters of non-indexed regions associated with coarse particles and regions of incomplete bonding remained as non-indexed points in the EBSD maps even after filtering. A critical misorientation angle of 2° was used for defining the boundary spacing and fractions of different boundary types in the EBSD maps. Low angle boundaries (LABs) were thus defined as those with misorientations in the range $2\text{--}15^\circ$. Boundaries with misorientations above 15° were defined as HABs. Furthermore, high misorientation regions (HMRs) and low misorientation regions (LMRs) [9,19,25] were identified in the EBSD maps to characterize heterogeneity in microstructural refinement in the as-

deformed sample. LMRs were defined as areas greater than $2.5 \mu\text{m}^2$ surrounded by boundaries with misorientations $>5^\circ$. The remaining areas in the deformed microstructure are defined as HMRs.

Fractions of texture components were calculated within a 15° deviation from the corresponding ideal orientations. Following our previous work [9], the rolling texture components after ARB is described as a combination of the Brass “Bs” $\{110\}\langle 112\rangle$, S $\{123\}\langle 634\rangle$, Copper “Cu” $\{112\}\langle 111\rangle$, and Dillamore “D” $\{4\ 4\ 11\}\langle 11\ 11\ 8\rangle$ orientations. Shear texture components are represented by the $\{100\}\langle 011\rangle$, $\{111\}\langle 011\rangle$, $\{111\}\langle 112\rangle$, and $\{112\}\langle 110\rangle$ components. In addition, grains of the cube $\{001\}\langle 100\rangle$ component are also analyzed in this work.

Recrystallized grains were defined based on an algorithm described in [26] using the following approach. First, a minimum angle of 1° (excluding twin $60^\circ \langle 111\rangle$ misorientations) was used to detect grains in the EBSD maps. Grains with an equivalent circular diameter (ECD) larger than $3 \mu\text{m}$ and partly surrounded by HABs were then considered to be recrystallized (see an example in the supplementary material). The orientation spread within these recrystallized grains was less than 1.5° .

The stored energy was calculated from the EBSD data using the method described in Ref.[27]. The specific boundary energy of the LABs was calculated from the Read-Shockley equation [28,29]. The specific boundary energy of HABs was taken as 0.866 J/m^2 [30].

Results

Deformed material

As reported in our previous publication [9], the texture of the ARB-processed Ni sample is heterogeneous through the thickness (see Fig. 2 and Table 1). Increased intensities of the D component and shear texture components are observed in the subsurface (see Fig. 1a), where the shear texture is

confined to the first 50–80 μm from the immediate surface. The summed fraction of the rolling texture components (f_{Rol}) in the subsurface layer is 48 %, which is much less than in the center and intermediate layers, where textures are more similar to the classical rolling-type texture (see Fig. 2b,c and Table 1).

An example of the deformed microstructure is shown in Fig. 3, covering an interface created in the center layer during the second rolling pass. The microstructure in the core (defined here as regions away from the bonding interface) is typical of the microstructure in heavily rolled nickel, where lamellar bands closely aligned with the rolling plane are combined with microshear bands at 25–40° to the RD [31,32] (see Fig. 3a). The microstructure within a volume extending over approximately 5 μm on either side across the interface is more refined and contains a larger frequency of HABs, which results in an increased frequency of HMRs (see Fig. 3b). The orientation map in Fig. 3c demonstrates that despite the very high rolling strain imposed during ARB, lamellae of the cube component and of random orientations are still present in the microstructure.

Interfaces also contain coarse particles (Fig. 4). The frequency of such particles appears to be higher along the interfaces created during the last two (fifth and sixth) passes (see Fig. 4a). Figure 4b, which presents the number of particles N_p coarser than 10 μm calculated per unit interface length, provides clear evidence that N_p increases with increasing number of rolling passes. An EDS analysis indicates that these particles contain a combination of chemical elements typical of stainless steels (Fig. 4d). The presence of these steel particles alters the microstructure around them, producing characteristic particle deformation zones (Fig. 4c). The microstructure in the particle deformation zones contains finer subgrains with a larger orientation spread than those in the core.

The sample-scale variations of the microstructure described previously in detail in Ref. [9] are summarized in Table 1 for the subsurface, intermediate and center layers. It is seen that the average

boundary spacing $d_{\theta>2^\circ}$ along the ND is fairly similar in all three layers, 155–160 nm. The differences in the average HAB spacing between the layers are more significant: the largest average HAB spacing is in the intermediate layer, 310 nm, whereas the subsurface layer is characterized by a considerably smaller average HAB spacing, 285 nm (see Table 1). Conversely, the lowest fraction of HMRs (f_{HMR}), 44 %, is in the intermediate layer, while the highest f_{HMR} , 61 %, is in the subsurface. The values of d_{HAB} and f_{HMR} in the center layer are in between the minimum and maximum values for the other two layers (see Table 1).

Table 1. Parameters characterizing the microstructure and crystallographic texture in the subsurface, intermediate and center layers of the deformed material.

Layer	f_{Rol} (%)	f_{Shear} (%)	$d_{\theta>2^\circ}$ (nm)	d_{HAB} (nm)	f_{HMR} (%)
Subsurface	48	17	160	285	61
Intermediate	82	2	156	310	44
Center	80	2	155	302	54

Annealed samples

EBSD maps from several samples annealed at 220 °C covering their entire sample thickness are shown in Fig. 5. It is seen that after 15 min the material is at an early stage of recrystallization (Fig. 5a), where the area fraction of recrystallized grains f_{Rex} in different layers is only 4–6 %. The average size of these recrystallized grains (d_{Rex}) is 6–7 μm , and many of them belong to the cube $\{001\}\langle 100\rangle$ texture (yellow in Fig. 5a). The EBSD map in Fig. 5a demonstrates that nucleation is not random, and that recrystallized grains appear preferentially at certain locations. Closer inspection reveals that nucleation takes place near bonding interfaces (see Fig. 6a) and around steel particles (see Fig. 6b and Fig. 7a). It

is noteworthy that nuclei in such places develop at some distance (typically greater than 1 μm) from either the bonding interface or the particle surface. This is especially pronounced at coarse steel particles, which appear to have a thin fine-structured shell resistant to nucleation, partially surrounded by a necklace consisting of a number of clustered recrystallized grains having different crystallographic orientations (Fig. 7a). Nuclei near the fifth and sixth interfaces are characterized by a greater variety of orientations than nuclei developed along other interfaces. Preferential nucleation is also observed in core regions, e.g. at shear bands (Fig. 7b) and within pre-existing cube lamellae (see Fig. 7c). In non-recrystallized areas, annealing results in structural coarsening: the average boundary spacing along the ND increases from ~ 160 nm before annealing to ~ 190 nm after 15 min of annealing, as measured within recovered regions in the intermediate layers, and to 220–250 nm as measured similarly in the subsurface and center layers.

The frequency, area fraction and average size of the recrystallized grains all increase with increasing annealing duration (see Fig. 5b,c and Fig. 8). After 30 min of annealing the intermediate layers contain the greatest area fraction of recrystallized grains ($f_{\text{Rex}}=44$ %) compared to the center and subsurface layers ($f_{\text{Rex}}=32$ % and 28 %, respectively). The difference in f_{Rex} between the layers is reduced after further annealing (see Fig. 8b). As seen in Figure 5c, there is a greater frequency of recrystallized grains having non-cube orientations near the surface and near the interfaces obtained by the last two (fifth and sixth) rolling passes than elsewhere.

After 210 min of annealing, recrystallization is almost complete ($f_{\text{Rex}}=95$ –97 %), with non-recrystallized areas mostly observed along the bonding interfaces, including regions in contact with steel particles (Fig. 9a,b). Such non-recrystallized regions appear to be more frequent along the interfaces introduced after the last two rolling passes than along the interfaces produced by the

preceding passes (Fig. 9c). The average recrystallized grain size in this almost fully recrystallized condition is approximately 10 μm in all layers (see Fig. 8a).

Recrystallization results in significant changes in texture (see Fig. 5 and Fig. 10), leading to strengthening of the cube components primarily at the expense of the rolling texture. There is no substantial difference between the center and intermediate layers in the evolution of texture, where the area fraction of the cube texture approaches 70 % after 210 min of annealing at 220 °C (see Fig. 10c). However, in the subsurface the cube texture is consistently weaker for each annealed condition.

Discussion

The origin of various heterogeneities of deformation texture and deformed microstructure in ARB-processed materials has been discussed in a number of previous publications [4–14]. Based on these publications, it can be summarized that sample-scale heterogeneities generally reflect the heterogeneous distribution of strain for the last few ARB cycles, whereas microscopic heterogeneities (i.e. the difference between the core and interface regions) are associated with the entire ARB process, where roll-bonding in each new cycle creates a new center layer with a new interface along two former surfaces. These interfaces contain coarse particles, which are morphologically similar in several ARB-processed materials [14–17]. In contrast to previous publications [14–17], where such coarse particles were either disregarded or described as oxide particles, the EDS analysis conducted in the present work provides clear evidence that these are steel particles. It is considered that these particles are imprinted fragments of the wire brush used for cleaning the surface before stacking and roll-bonding. The number of such particles per unit interface length is largest for the recently formed fifth and sixth interfaces (Fig. 4b) because the distance between particles imprinted into each newly created interface increases with increasing strain imposed by subsequent passes. An additional factor which may contribute to the

larger N_p for the interfaces formed during the last two cycles is that material hardening during the ARB process may result in a higher likelihood of brush wire breaking in contact with a hardened surface compared to the softer surface after only a small number of rolling passes. The influence of such microscopic heterogeneities, as well as sample-scale heterogeneities, on the recrystallization process will be considered in the following subsections.

Microscopic heterogeneities

The presence of microscopic heterogeneities in the form of a highly refined microstructure at the interfaces between bonded layers, particle deformation zones and shear bands greatly affects the recrystallization behavior of the ARB-processed nickel sample, such that these deformation heterogeneities along with cube-oriented lamellae provide preferential nucleation sites during annealing (see Fig. 6a, Fig. 7 and Fig. 8).

The high frequency of recrystallized grains near the interface layers, which are characterized by increased concentrations of HMRs before annealing (see Fig. 3b), is consistent with previous observations of preferential nucleation within HMRs in other heavily deformed materials [19,24,25]. Calculations made based on the EBSD data, indicate that in the deformed microstructure the stored energy within a 10 μm -wide region across the interface is approximately 10 % higher than in the core. This higher stored energy provides a higher driving force for nucleation, which results in a large number of recrystallized grains along the interface at the early stage of recrystallization.

Furthermore, particle deformation zones, which are also preferential sites for nucleation, are also located along the interface and thus additionally contribute to near-interface nucleation. Due to the large variety of crystallographic orientations in the particle deformations zones (Fig. 7a), the orientations of recrystallized grains nucleated within these zones are also different [30]. As there is a

higher frequency of particles along the fifth and sixth interfaces, these last interfaces contain a larger frequency of non-cube oriented grains than the other interfaces (see Fig. 5c). Another reason for the more varied orientations of recrystallized grains along the fifth and sixth interfaces is that the texture along these “fresh” interfaces is slightly different than the texture along the older interfaces. Analysis of the deformation texture within 10 μm across the fifth and sixth interfaces indicates that the fraction of the rolling texture here is approximately 10 % lower than the overall fraction of this texture in the center and intermediate layers. Apparently, this lower fraction reflects the influence of increased shear at the surface before bonding by the fifth and sixth rolling passes, and additionally contributes to the greater orientation variety of recrystallized grains along those interfaces. Due to the increased frequency of nuclei near the interface, these interface regions contain a larger frequency of small grains than the core (see Fig. 5c and Fig. 9c). The latter is in agreement with previous findings for copper annealed after ARB [22].

The fact that despite the high driving force for recrystallization, both the immediate interface surface and a thin shell around coarse particles are resistant to nucleation can be attributed to possible contamination by iron and chromium present in the steel brush (see Fig. 4b). Some of these regions remain non-recrystallized even after 210 min of annealing 220 $^{\circ}\text{C}$ (Fig. 9). Similar non-recrystallized regions along the bonding interface in Ni were observed by Kwan et al. [23] in Al, though in their work these regions were described as “discontinuous segregations of small grains”. Our analysis clearly indicates that such regions are remnants of the lamellar structure produced during deformation.

Sample-scale heterogeneities

In addition to the differences in the recrystallization behavior induced by microscopic heterogeneities, there are appreciable differences between subsurface, intermediate and center layers in the progress of

recrystallization (in particular, after 30 min of annealing) and in the development of the cube texture (see Fig.8b and Fig.10c). The observation that the subsurface layer, which has an initially high f_{HMR} (see Table 1), recrystallizes more slowly than the intermediate layer with an initially much lower f_{HMR} , may look unexpected and deserves additional analysis. To rationalize the difference in the annealing behavior between the layers, we again consider the influence in turn of the stored energy and the crystallographic texture.

Influence of the stored energy

The values of the stored energy E_s calculated from the EBSD data for the different layers in the as-deformed material are fairly similar (blue bars in Fig. 11a), consistent with the observed similar fractions recrystallized in the first annealed sample (i.e. after 15 min of annealing, see Fig. 8b and blue bars in Fig. 11b). For the 15 min sample the E_s values (red bars in Fig. 11a), calculated only for non-recrystallized (recovered) areas, are both lower than those in the as-deformed sample, and are noticeably different for the different layers, being considerably larger in the intermediate layers than in the center and subsurface layers. The higher stored energy in the recovered microstructure of the intermediate layers implies that the driving force for recrystallization is also higher in these layers, which explains the significantly higher values of f_{ReX} after 30 min of annealing in these layers (see Fig. 8b and red bars in Fig. 11b).

Considering possible correlations between f_{HMR} and f_{ReX} , it is suggested that initially higher f_{HMR} values in particular layers of the as-deformed material do not necessarily result in higher f_{ReX} values in the same layers after annealing because the deformed microstructure evolves during recovery. Recovery, either prior to the onset of recrystallization or otherwise taking place concurrently with recrystallization, typically leads to structural coarsening, which can substantially modify the local microstructure [20,33–35]. Such coarsening is expected to be more pronounced in HMRs than in LMRs

as the former contain a greater frequency of highly mobile HABs. Therefore, during the first 15 min of annealing the microstructure in the center and subsurface layers with higher HMR fractions coarsens more (to 220–250 nm as measured along the ND) than in the intermediate layer (to 190 nm along the ND), where the fraction of HMRs was initially lower (see Table 1). These significant changes underline the importance of characterizing the recovered state when analyzing recrystallization. Another reason which contributes to differences in the progress of recrystallization in the different layers is crystallographic texture, as considered in the following subsection.

Effects of crystallographic texture

In agreement with crystal plasticity modelling results [7], our ARB Ni sample demonstrates a strong through-thickness variation of the crystallographic texture (see Fig. 2 and Table 1). In the center and intermediate layers, the deformation texture resembles the classical rolling texture with a summed area fraction of the Bs, S and Cu components of 74–76 %, which is similar to that observed in other Ni samples cold rolled to a similar strain [36]. Therefore, the texture evolution during annealing in these layers is expected to be similar to that in conventionally rolled (CR) Ni, where a strong cube texture typically develops upon annealing. In rolled *fcc* materials with a low and medium stacking fault energies, cube-oriented grains have been reported to nucleate from pre-existing cube lamellae [37–39] and, in some cases, may also be produced by annealing twinning [40]. Such nucleation examples have also been found in our work (see e.g. Fig. 7a,c). As cube-oriented grains generally grow faster than grains of other orientations [36], they win the growth competition with other grains, which results in a strong cube texture during recrystallization. For example, in Ni conventionally rolled to $\varepsilon_{VM} = 4.5$ and recrystallized at 300 °C, the fraction of the cube texture was ~70 % [36,41]. This fraction is very similar to the values obtained in the center and intermediate layers of our ARB-processed sample when recrystallization was almost complete. Thus, except for regions near the fresh interfaces, the

development of the recrystallization texture the center and intermediate layers of ARB-processed Ni is, in general, fairly similar to that typically reported for CR Ni [36,41].

In contrast, the fraction of the cube component in the subsurface is only 55 %. This reduced fraction of the cube texture can be attributed to the reduced strength of the classical rolling texture. Indeed, for the deformed sample, the summed area fraction of the rolling texture components (calculated excluding the D component) in the subsurface is only half of that in the center and intermediate layers. Intensities of the D and shear texture components in the subsurface are, however, increased (see Fig. 2a). Thus, the environment in which cube-oriented grains nucleate and grow in the subsurface is different from that in the other layers. The texture effect is especially pronounced within the first 50-80 μm -thick sublayer with the strongest shear components. This is illustrated in Fig. 12, where distributions of misorientations between the ideal cube orientation and measured orientations within the deformed matrix are presented for the first 80 μm from the immediate surface and for the center layer (the latter distribution is also similar to that for the intermediate layers).

It is seen that both distributions in Fig. 12 are characterized by high frequencies of misorientation angles between $\sim 40^\circ$ and $\sim 55^\circ$ and thus are not significantly different. However, the distribution of misorientation axes in Fig. 12a is very different from that in Fig. 12b. Whereas there is a high density of axes around the $\langle 111 \rangle$ pole in the cube/matrix misorientation distribution for the center layer (see Fig. 12b), this distribution for the regions with increased shear texture is much broader and the density near $\langle 111 \rangle$ is low (see Fig. 12a). In a previous study of recrystallization in heavily rolled Ni [42], it was found that grains surrounded by high angle boundaries with misorientation axes near $\langle 111 \rangle$ were favorable for growth. This observation is consistent with the present experimental results, where a

stronger cube-texture is developed in the center regions compared to the subsurface, given the observed differences in rotation axes for these two regions (Fig. 12).

Analysis of recrystallization kinetics and comparison with conventionally rolled Ni

When analyzing samples produced using the ARB process, it is useful to consider how these samples differ from those produced by conventional rolling. In our previous work [3], such a comparison was made for ARB and CR samples after a strain of 2.4, where it was found that the microstructure in the ARB sample was on average finer than that after conventional rolling. This greater refinement by ARB appears to hold also for the strain level applied for the sample studied in the present work. For example, Zhang et al. [41] reported $d_{\text{HAB}} = 0.53 \mu\text{m}$ for Ni rolled to a similar strain of $\varepsilon_{\text{VM}} = 4.5$. Table 1 shows that this parameter is much smaller, $\sim 0.3 \mu\text{m}$, in the ARB sample investigated here. To analyze what differences exist in the annealing behavior of the ARB and CR samples, it is convenient to compare their recrystallization kinetics using a standard Johnson-Mehl-Avrami-Kolmogorov (JMAK) plot, presenting $-\ln(1 - f_{\text{Rex}})$ as a function of annealing time t on a double logarithmic scale. Assuming that $f_{\text{Rex}} = 1 - \exp(-Kt^n)$, where K is a constant, the exponent n , frequently referred to as Avrami exponent, can be derived from the slope in the JMAK plot. This plot is shown in Fig. 13a, presenting the overall evolution for the entire sample, ~~as the differences between different layers are small~~. It is seen that the slope decreases continually as recrystallization proceeds, and accordingly that the standard JMAK equation does not describe well this kinetics. A negative deviation of the JMAK-plot from a straight line is not surprising, as similar behavior has also been seen in other materials, e.g. rolled copper [43,44]. Several reasons could lead to such a deviation, including both a non-uniform distribution of nucleation sites and non-uniform growth of the nuclei.

To analyze the change in slope of the JMAK-plot with annealing time, the data have been fitted to a fourth order polynomial, $\log(-\ln(1 - V_v)) = A + B \log t + C(\log t)^2 + D(\log t)^3 + E(\log t)^4$, where A to E are

fitting parameters. It should be noted that the three extra terms of high order $\log t$ are only used to obtain a good fit to the experimental data and do not have a physical interpretation [43]. Based on this approach, the Avrami exponent n is determined to be 3.5, 2.4, 0.7 and 0.02 at 15, 30, 90 and 210 min, respectively.

The standard JMAK model assumes that the nuclei are randomly distributed. With the further assumption that all recrystallized grains grow in 3D with a constant linear growth rate, an Avrami exponent of $n = 3$ corresponds to site-saturated nucleation and $n = 4$ corresponds to a constant nucleation rate [45]. In the early stage of recrystallization (≤ 15 min), although the nuclei are not distributed randomly throughout the sample thickness, many nuclei can grow freely in 3D. Considering the data in Fig.13b, which shows the number of recrystallized grains N_v , calculated as $N_v = N_a/R$, where the N_a is the number of grains per unit area, and R is the average grain size, it is evident that the nucleation rate is somewhere between the two ideal cases of a constant nucleation rate and site saturation. Therefore, the Avrami exponent of $n = 3.5$ is reasonable for the very early stages of recrystallization. As recrystallization proceeds, the non-random distribution of nuclei leads to an increasing effect of impingement [46]. According to [43], such impingement can reduce the growth from 3D to 2D, or even to 1D, at the later stage of recrystallization, with a corresponding decrease in the Avrami exponent. Such a decrease in the growth dimension explains partly the decrease of the Avrami exponent observed in the present work.

In addition to the effect of impingement on the growth dimension, changes in the growth rate during recrystallization can also lead to a reduction in the Avrami exponent [47]. To evaluate this effect, the average growth rate $\langle G \rangle$ of recrystallized grains was calculated using the extended Cahn-Hagel method [48], in which the measured growth rate is isolated from the effect of impingement by only considering the migration of boundaries where impingement does not take place. As shown in

Fig.13c, the average growth rate is initially high, but decreases as the recrystallization proceeds. These changes in $\langle G \rangle$ and N_v observed in our material are very different from those reported for nickel rolled to $\varepsilon_{vM} = 4.5$, where both $\langle G \rangle$ and N_v were found almost constant during annealing [36]. The observed decrease in the growth rate is mainly due to the fact that the stored energy within the non-recrystallized areas is reduced with increasing annealing duration. It is postulated also that regions near the bonding interfaces may become contaminated during the ARB process, and that the growth rate in these regions is additionally affected by impurities. This is supported by the observation that the extremely slow process at the end of recrystallization is mainly related to the regions along the bonding interfaces specific to the ARB process (Fig. 9).

Conclusions

Investigation using EBSD and BSE imaging reveals that deformation of nickel by ARB to a von Mises strain of 4.8 introduces heterogeneity over a wide range of length scale. At the microscopic scale heterogeneities are mostly associated with regions near the bonding interface that are more refined and contain a higher stored energy than elsewhere. These regions also contain particle deformation zones around coarse steel particles introduced during the ARB process. Sample-scale heterogeneities are seen as variations in the fractions of rolling and shear texture components and in the relative fractions of high misorientation regions in the subsurface, intermediate and center layers. During annealing at 220 °C these heterogeneities influence the recrystallization in a complex manner with the following key points identified:

- 1) Nucleation of recrystallized grains takes place preferentially both at regions of higher stored energy near bonding interfaces, and deformation zones around coarse particles, identified as arising from wire-brushing of the surface prior to each bonding cycle, as well as from shear bands

and cube bands elsewhere in the microstructure. The heterogeneity in nucleation extends to the sample scale as a result of the variation in particle density per unit area of each bonding interface.

- 2) The fraction of the cube texture and the average size of recrystallized grains are smaller in the subsurface than in the other layers. The difference in the recrystallization texture can be attributed to the stronger shear texture, and correspondingly weaker rolling texture, produced by rolling in the subsurface layers. Additionally, sample-scale heterogeneity, amplified by a significant reduction in stored energy during recovery that takes place to a lesser extent in the intermediate layer, results in faster recrystallization in this layer compared to the other layers. These significant changes underline the importance of characterizing the recovered state when analyzing recrystallization.
- 3) Both the microscale and sample-scale heterogeneities resulting from the ARB process lead to recrystallization kinetics significantly different to those reported previously for conventionally rolled Ni deformed to a similar strain. In contrast to the conventionally rolled nickel sample, where the number of recrystallized grains and their growth rate were found to be almost constant during annealing, nucleation in the present ARB sample takes place over an extended period of time with the growth rate of recrystallizing grains decreasing with time.

The investigation highlights the sensitivity of recrystallization in terms of both nucleation and growth to microstructural heterogeneities and the importance, particularly in metals deformed to large strains, of the effect of recovery in establishing the pattern of heterogeneity in which recrystallization takes place. In this regard, ARB-processed samples provide a rich microstructural environment for the study of such effects.

Acknowledgements: The authors are grateful to Professor D. Juul Jensen and Dr. F.X. Lin for useful discussions. The authors acknowledge the support from the Danish National Research Foundation (Grant DNRF86-5) and the National Natural Science Foundation of China (Grant 51261130091).

References

- [1] Saito Y, Tsuji N, Utsunomiya H, Sakai T, Hong RG (1998) Ultra-fine grained bulk aluminum produced by accumulative roll-bonding (ARB) process. *Scr Mater* 39:1221–1227
- [2] Saito Y, Utsunomiya H, Tsuji N, Sakai T (1999) Novel ultra-high straining process for bulk materials – development of the accumulative roll-bonding (ARB) process. *Acta Mater* 47:579–583
- [3] Zhang YB, Mishin OV, Kamikawa N, Godfrey A, Liu W, Liu Q (2013) Microstructure and mechanical properties of nickel processed by accumulative roll bonding. *Mater Sci Eng A* 576:160–166
- [4] Heason CP, Prangnell PB (2002) Grain refinement and texture evolution during the deformation of Al to ultra-high strains by accumulative roll bonding (ARB). *Mater Sci Forum* 396-402:429–434
- [5] Kim HW, Kang SB, Tsuji N, Minamino Y (2005) Deformation textures of AA8011 aluminum alloy sheets severely deformed by accumulative roll bonding. *Metall Mater Trans A* 36:3151–3163
- [6] Kamikawa N, Tsuji N, Huang X, Hansen N (2007) Through-thickness characterization of microstructure and texture in high purity aluminum processed to high strain by accumulative roll-bonding. *Mater Trans* 48:1978–1985
- [7] Li S, Sun F, Li H (2010) Observation and modeling of the through-thickness texture gradient in commercial-purity aluminum sheets processed by accumulative roll-bonding. *Acta Mater* 58:1317–1331

- [8] Su L, Lu C, Gazder AA, Saleh AA, Deng G, Tieu K, Li H (2014) Shear texture gradient in AA6061 aluminum alloy processed by accumulative roll bonding with high roll roughness. *J Alloys Compd* 594:12–22
- [9] Zhang YB, Mishin OV, Godfrey A (2014) Analysis of through-thickness heterogeneities of microstructure and texture in nickel after accumulative roll bonding. *J Mater Sci* 49:287–293
- [10] Najafzadeh N, Quadir MZ, Munroe P (2015) Through thickness microstructural and texture inhomogeneity within Al layers in ARB-produced Al-Al(Sc) layered composite sheets. *Metall Mater Trans A* 46:4772–4782
- [11] Lee SH, Saito Y, Tsuji N, Utsunomiya H, Sakai T (2002) Role of shear strain in ultragrain refinement by accumulative roll-bonding (ARB) process. *Scr Mater* 46:281–285
- [12] Lee SH, Saito Y, Tsuji N, Utsunomiya H, Sakai T (2002) Microstructures and mechanical properties of 6061 aluminum alloy processed by accumulative roll-bonding. *Mater Sci Eng A* 325:228–235
- [13] Duan JQ, Quadir MZ, Ferry M (2016) An analytical framework for predicting the limit in structural refinement in accumulative roll bonded nickel. *Metall Mater Trans A* 47:471–478
- [14] Su L, Lu C, Li H, Deng G, Tieu K (2014) Investigation of ultrafine grained AA1050 fabricated by accumulative roll bonding. *Mater Sci Eng A* 614:148–155
- [15] Xing ZP, Kang SB, Kim HW (2001) Softening behavior of 8011 alloy produced by accumulative roll bonding. *Scr Mater* 45:597–604
- [16] Kamikawa N, Tsuji N, Mi Y (2004) Microstructure and texture through thickness of ultralow carbon IF steel sheet severely deformed by accumulative roll-bonding. *Sci. Technol. Adv. Mater.* 5:163–172

- [17] Pirgazi H, Akbarzadeh A, Petrov R, L. Kestens L (2008) Microstructure evolution and mechanical properties of AA1100 aluminum sheet processed by accumulative roll bonding. *Mater Sci Eng A* 497:132–138
- [18] Kim J-K, Jee Y-K, Huh M-Y (2004) Formation of textures and microstructures in asymmetrically cold rolled and subsequently annealed aluminum alloy 1100 sheets. *J Mater Sci* 39:5365–5369
- [19] Mishin OV, Bowen JR (2009) Through-thickness variations of deformed and annealed microstructures in ECAE-processed copper. *Metall Mater Trans A* 40:1684–1692
- [20] Mishin OV, Godfrey A, Juul Jensen D, Hansen N (2013) Recovery and recrystallization in commercial purity aluminum cold rolled to an ultrahigh strain. *Acta Mater* 61:5354–5364
- [21] Lin FX, Zhang YB, Tao N, Pantleon W, Juul Jensen D (2014) Effects of heterogeneity on recrystallization kinetics of nanocrystalline copper prepared by dynamic plastic deformation. *Acta Mater* 72:252–261
- [22] Suresh KS, Rollett AD, Suwas S (2013) Evolution of microstructure and texture during deformation and recrystallization of heavily rolled Cu-Cu multilayer. *Metall Mater Trans A* 44:3866–3881
- [23] Kwan C, Wang Z, Kang S-B (2008) Mechanical behavior and microstructural evolution upon annealing of the accumulative roll-bonding (ARB) processed Al alloy 1100. *Mater Sci Eng A* 480:148–159
- [24] Godfrey A, Mishin OV, Yu T (2015) Characterization and influence of deformation microstructure heterogeneity on recrystallization. *IOP Conf Ser: Mater Sci Eng* 89:012003
- [25] Zhang HW, Luo ZP, Hansen N, Lu, Influence of structural heterogeneity on the structural coarsening during annealing of polycrystalline Ni subjected to dynamic plastic deformation. *IOP Conf Ser: Mater Sci Eng* 89: 012056

- [26] Wu GL, Juul Jensen D (2008) Automatic determination of recrystallization parameters based on EBSD mapping. *Mater Charact* 59:794–800
- [27] Godfrey A, Cao WQ, Hansen N, Liu Q (2005) Stored energy, microstructure, and flow stress of deformed metals. *Metall Mater Trans A* 36:2371–2378
- [28] Read WT, Shockley W (1950) Dislocation models of crystal grain boundaries. *Phys Rev* 78:275–289
- [29] Read WT (1953) *Dislocation in Solids*. McGraw-Hill, New York, pp 155–172
- [30] Humphreys FJ, Hatherly M (2004) *Recrystallization and Related Annealing Phenomena* (2nd edition). Elsevier Ltd, Oxford
- [31] Hughes DA, Hansen N (1993) Microstructural evolution in nickel during rolling from intermediate to large strains. *Metall Trans A* 24:2021–2037
- [32] Hughes DA, Hansen N (2000) Microstructure and strength of nickel at large strains. *Acta Mater* 48:2985–3004
- [33] Xing Q, Huang X, Hansen N (2006) Recovery of heavily cold-rolled aluminum: Effect of local texture. *Metall Mater Trans A* 37:1311–1322
- [34] Zhang ZB, Tao NR, Mishin OV, Pantleon W (2016) Oxide dispersion-strengthened steel PM2000 after dynamic plastic deformation: nanostructure and annealing behavior. *J Mater Sci* 51:5545–5555
- [35] Zhang ZB, Zhang YB, Mishin OV, Tao NR, Pantleon W, Juul Jensen D (2016) Analysis of orientation-dependent recovery and recrystallization in a modified 9Cr-1Mo steel deformed by compression at a high strain rate. *Metall Mater Trans A* 47: 4682– 4693
- [36] Li XL, Liu W, Godfrey A, Juul Jensen D, Liu Q (2007) Development of the cube texture at low annealing temperatures in highly rolled pure nickel. *Acta Mater* 55:3531–3540

- [37] Ridha AA, Hutchinson WB (1982) Recrystallisation mechanisms and the origin of cube texture in copper. *Acta Metall* 30:1929–1939
- [38] Samajdar I, Verlinden B, Rabet L, Van Houtte P (1999) Recrystallization texture in a cold rolled commercial purity aluminum: on the plausible macro- and micro-mechanisms. *Mater Sci Eng A* 266:146–154
- [39] Zaefferer S, Baudin T, Penelle R (2001) A study on the formation mechanisms of the cube recrystallization texture in cold rolled Fe–36 %Ni alloys. *Acta Mater* 49:1105–1122
- [40] Duggan BJ, Sindel M, Köhlhoff GD, Lücke K (1990) Oriented nucleation, oriented growth and twinning in cube texture. *Acta Metall Mater* 38:103–111
- [41] Zhang YB, Godfrey A, Juul Jensen D (2009) Effects of strain on recrystallization of nickel metals and nanometals produced by heavy cold rolling, in: *Risø Int Symp on Mater Sci 30*, DTU, Roskilde, pp 423–430
- [42] Zhang YB, Godfrey A, Liu Q, Liu W, Juul Jensen D (2009) Analysis of the growth of individual grains during recrystallization in pure nickel. *Acta Mater* 57:2631–2639
- [43] Vandermeer RA, Juul Jensen D (1995) Quantifying recrystallization nucleation and growth kinetics of cold-rolled copper by microstructural analysis. *Metall Mater Trans A* 26:2227–2235
- [44] Lin FX, Zhang YB, Pantleon W, Juul Jensen D (2015) Supercube grains leading to a strong cube texture and a broad grain size distribution after recrystallization. *Phil. Mag* 22:2427–2449
- [45] Johnson WA, Mehl RF (1939) Reaction kinetics in processes of nucleation and growth. *Trans AIME* 135:416–430
- [46] Tong WS, Rickman JM, Barmak K (1999) Quantitative analysis of spatial distribution of nucleation sites: microstructural implications. *Acta Mater* 47:435–445

[47] Godiksen RB, Schmidt S, Juul Jensen D (2007) Effects of distributions of growth rates on recrystallization kinetics and microstructure. *Scr Mater* 57:345–348

[48] Juul Jensen D (1992) Growth of nuclei with different crystallographic orientations during recrystallization. *Scr Metall Mater* 27:533–538

Figure captions

Fig. 1 Definition of layers and interfaces in the ARB-processed Ni sample. Numbers correspond to the rolling pass number, during which an interface was produced. Dotted lines with no number correspond to the interfaces obtained during the second rolling pass.

Fig. 2. {111} pole figures showing crystallographic textures in different layers of the ARB-processed Ni sample: (a) subsurface; (b) intermediate layer and (c) center layer. (a) and (b) show data from just one side of the sample. Each pole figure represents orientations measured in an area of $\sim 0.3 \text{ mm}^2$. Contour lines: 1, 2, 3, 5 times random.

Fig. 3. EBSD maps showing the microstructure in a region across the interface in the center layer created during the second rolling pass (marked by arrows): (a) grain boundary map; (b) HMR/LMR map; (c) orientation map. HABs are shown as black lines. LABs are shown as grey lines in (a) and white lines in (b,c). The RD is parallel to the scale bar.

Fig. 4. Steel particles imprinted along the interfaces: (a) secondary electron SEM image showing the spatial distribution of particles; (b) the number of coarse ($>10 \mu\text{m}$ along RD) particles N_p per unit interface length as a function of the rolling pass number; (c) BSE image showing a particle and a characteristic particle deformation zone; (d) EDS spectrum from the center of the particle in (c). Dashed lines and the numbers in (a) indicate the interfaces obtained during the last two (fifth and sixth) rolling passes.

Fig. 5. Orientation maps showing the microstructure through the entire thickness of the samples annealed at $220 \text{ }^\circ\text{C}$ for (a) 15 min; (b) 30 min; (c) 90 min. Arrows mark the bonding interface along the mid-thickness. Dashed lines and the numbers in (c) indicate the interfaces during the last two (fifth and

sixth) rolling passes. LABs, HABs and twin boundaries are shown as white, black and purple lines, respectively. The RD is parallel to the scale bar.

Fig. 6. BSE images showing recrystallized grains nucleated near interfaces in the sample annealed at 220 °C for 15 min: (a) along the interface; (b) around a coarse steel particle lying at a bonding interface. The RD is parallel to the scale bar.

Fig. 7. Orientation maps showing nuclei and recrystallized grains after 15 min of annealing at 220 °C: (a) grains of different orientations nucleated around a coarse steel particle (seen as a black region). Colored pixels seen inside the particle are indexed as nickel, most likely introduced as an artifact during sample preparation by smearing of material onto the exposed particle surface; (b) at a shear band (marked by an arrow); (c) in core regions by bulging out from a pre-existing cube band. LABs, HABs and twin boundaries are shown as white, black and purple lines, respectively. The RD is parallel to the scale bar.

Fig. 8. The average size (a) and area fraction (b) of recrystallized grains developed in the ARB-processed Ni sample during annealing at 220 °C. The error bars correspond to the standard deviation for the data averaged over several regions in each layer.

Fig. 9. Microstructure of the ARB-processed Ni sample annealed at 220 °C for 210 min: (a,b) BSE images showing non-recrystallized areas along the interface (a) and adjacent to a steel particle (b). (c) orientation map from the center layer, where LABs, HABs and twin boundaries are shown as white, black and purple lines, respectively. In (c) dashed lines and numbers indicate the interfaces and the corresponding rolling pass numbers when these interfaces were produced. The RD is parallel to the scale bar.

Fig. 10. Changes in the fractions of different texture components in ARB-processed Ni during annealing at 220 °C: (a) rolling texture; (b) shear texture; (c) cube texture.

Fig. 11. Correlation between the stored energy in the deformed/recovered microstructures and fraction recrystallized after subsequent annealing at 220 °C: (a) stored energy calculated from the EBSD data for the as-deformed sample and for the recovered regions after 15 min of annealing; (b) f_{ReX} after 15 min and 30 min of annealing.

Fig. 12. Distributions of misorientations between the ideal cube orientation and orientations measured in the deformation matrix in different layers: (a) within first 80 μm from the immediate surface of the ARB sample; (b) in the center layer.

Fig. 13. Parameters of recrystallization in the entire ARB sample annealed at 220 °C: (a) JMAK plot; (b) total number of recrystallized grains N_v ; (c) growth rate $\langle G \rangle$. The error bars in (a) represent the standard deviation for the data, averaged over the center, intermediate and subsurface layers.

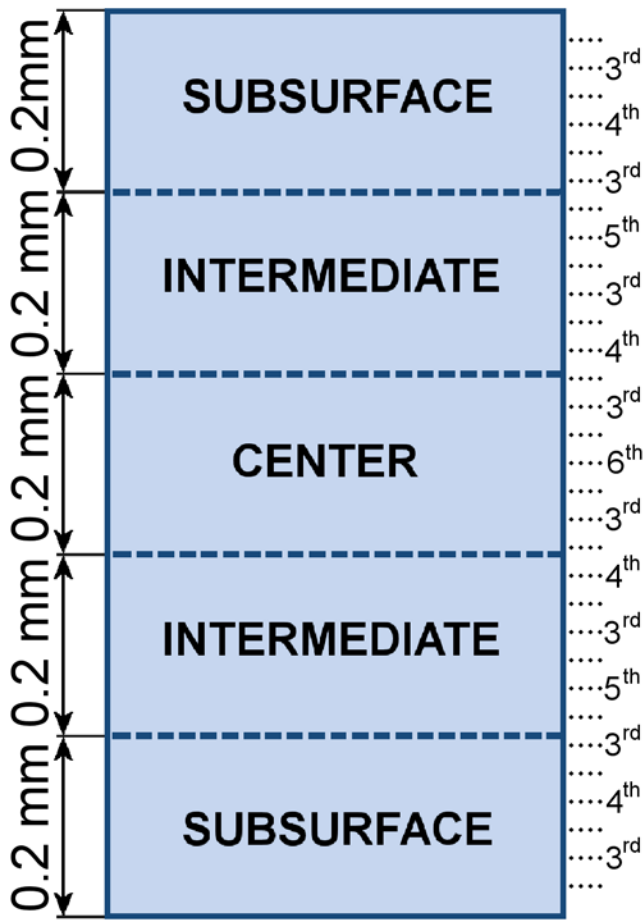


Fig.1

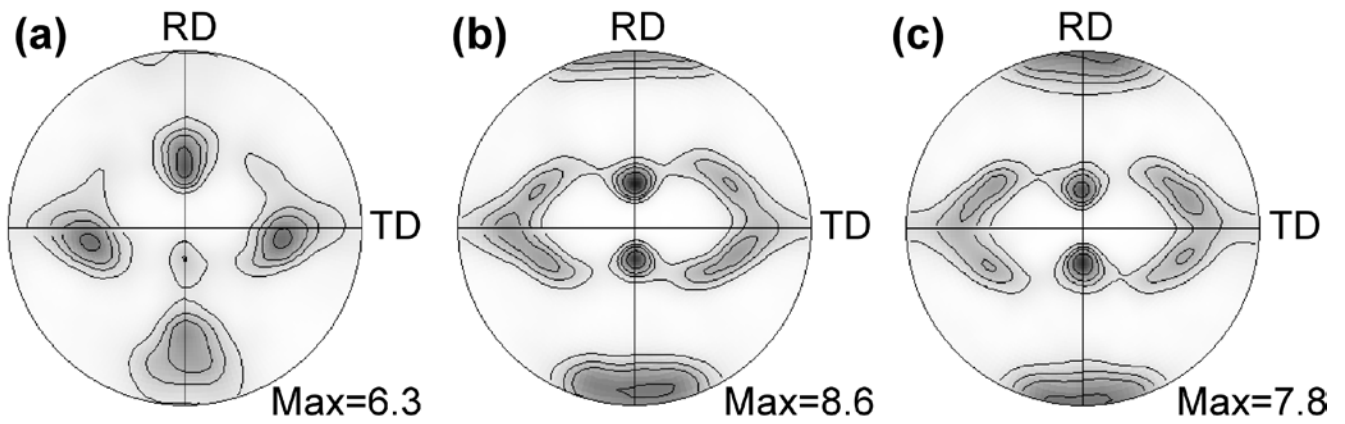


Fig.2

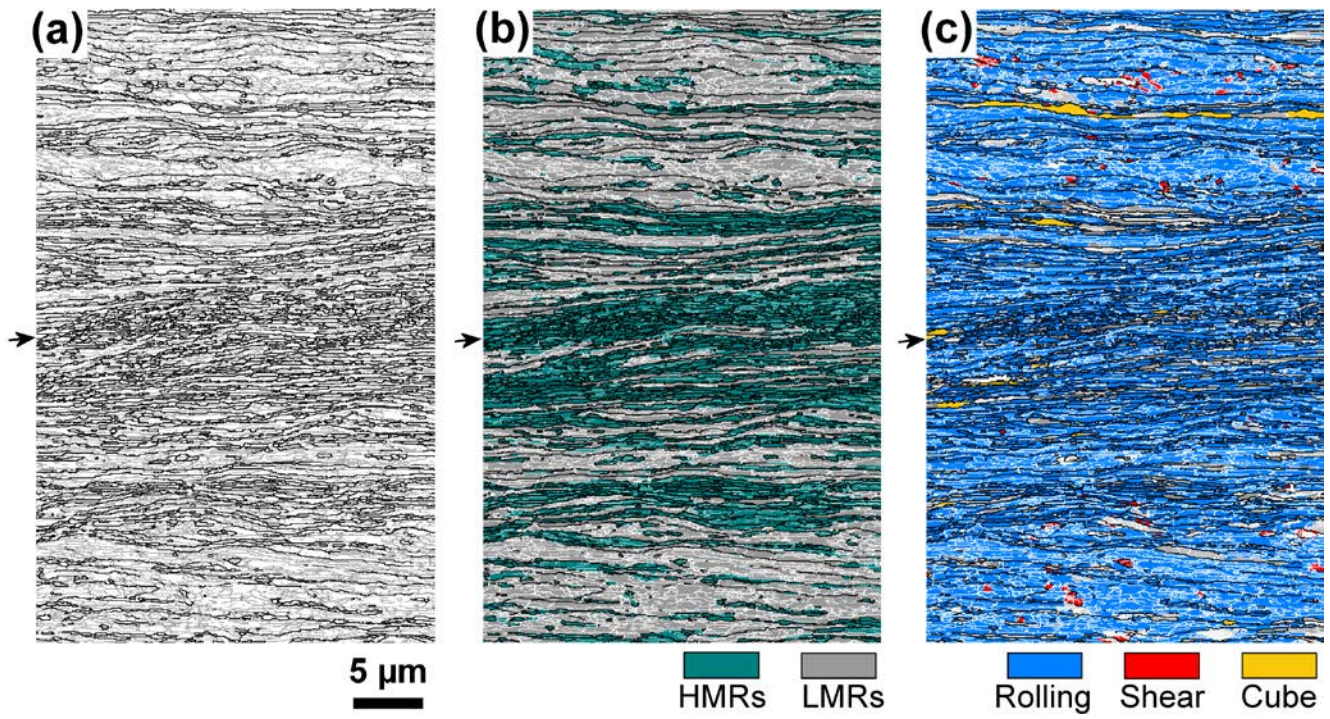


Fig.3

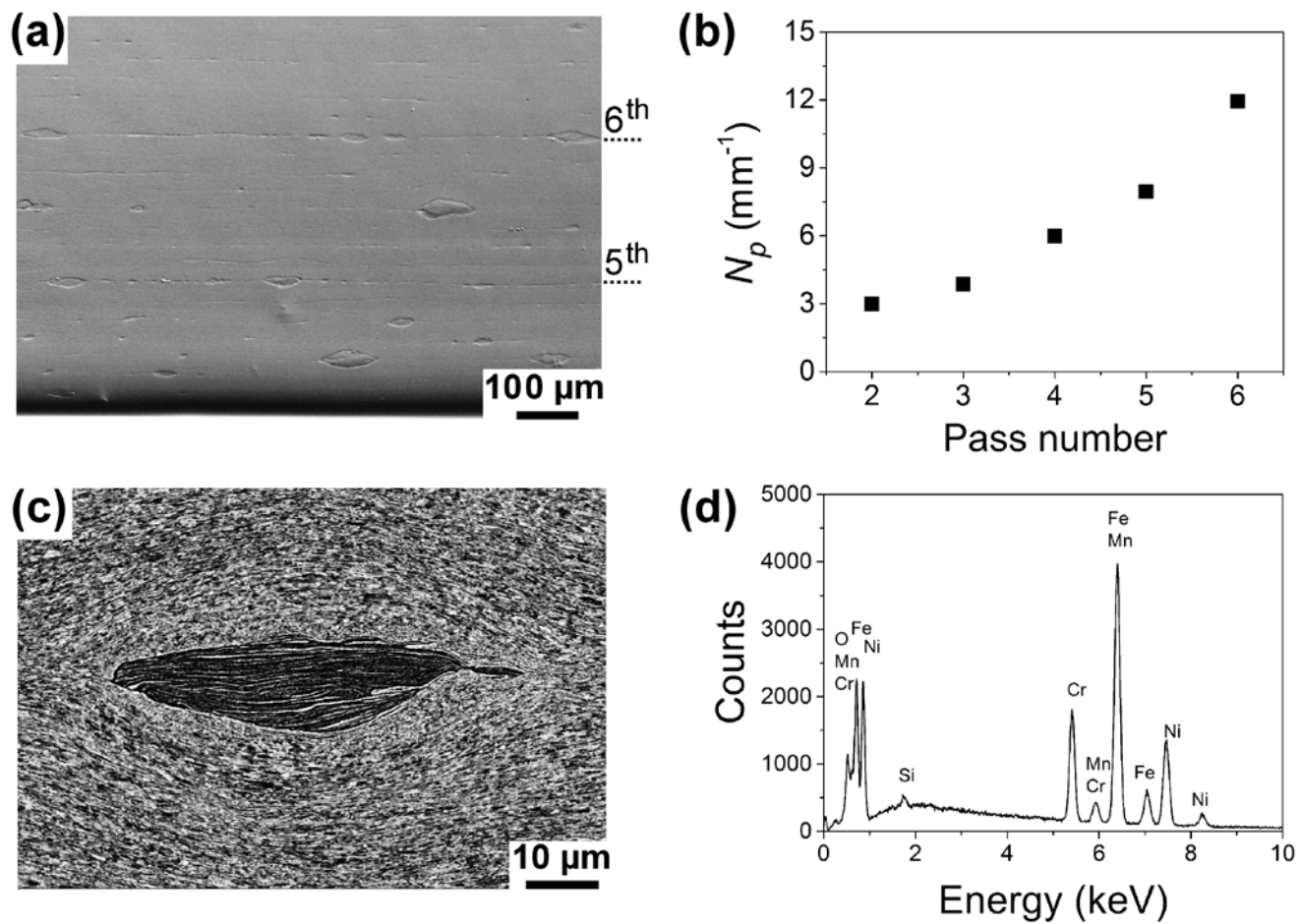


Fig.4

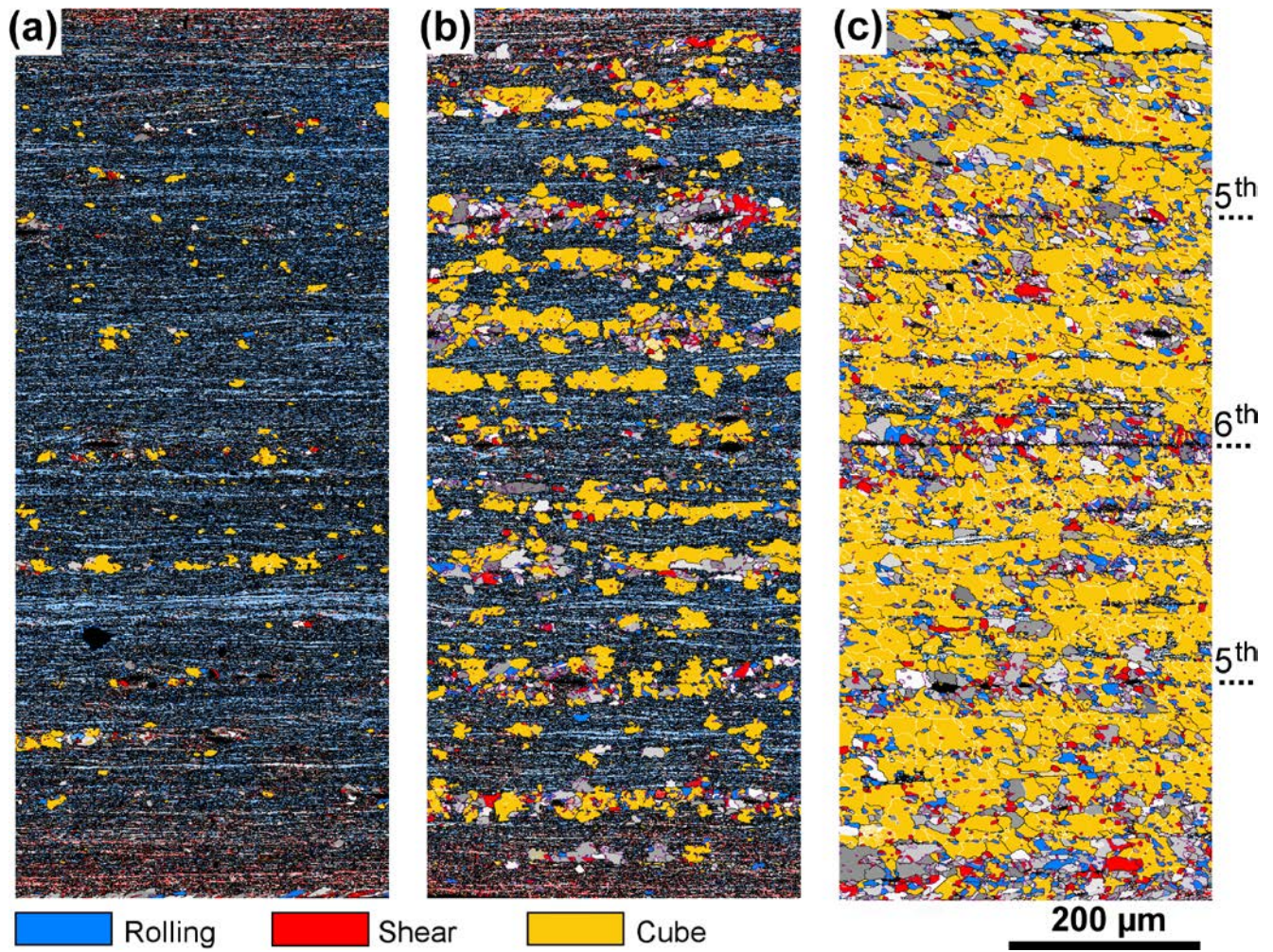


Fig.5

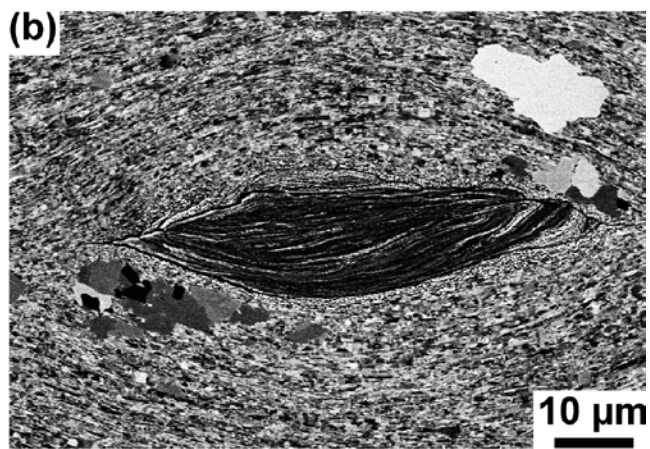
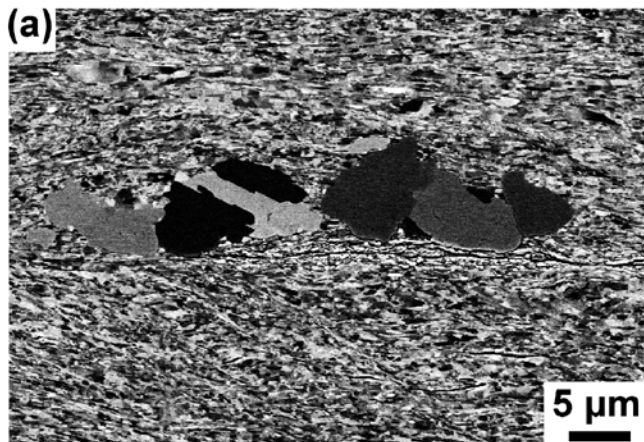


Fig.6

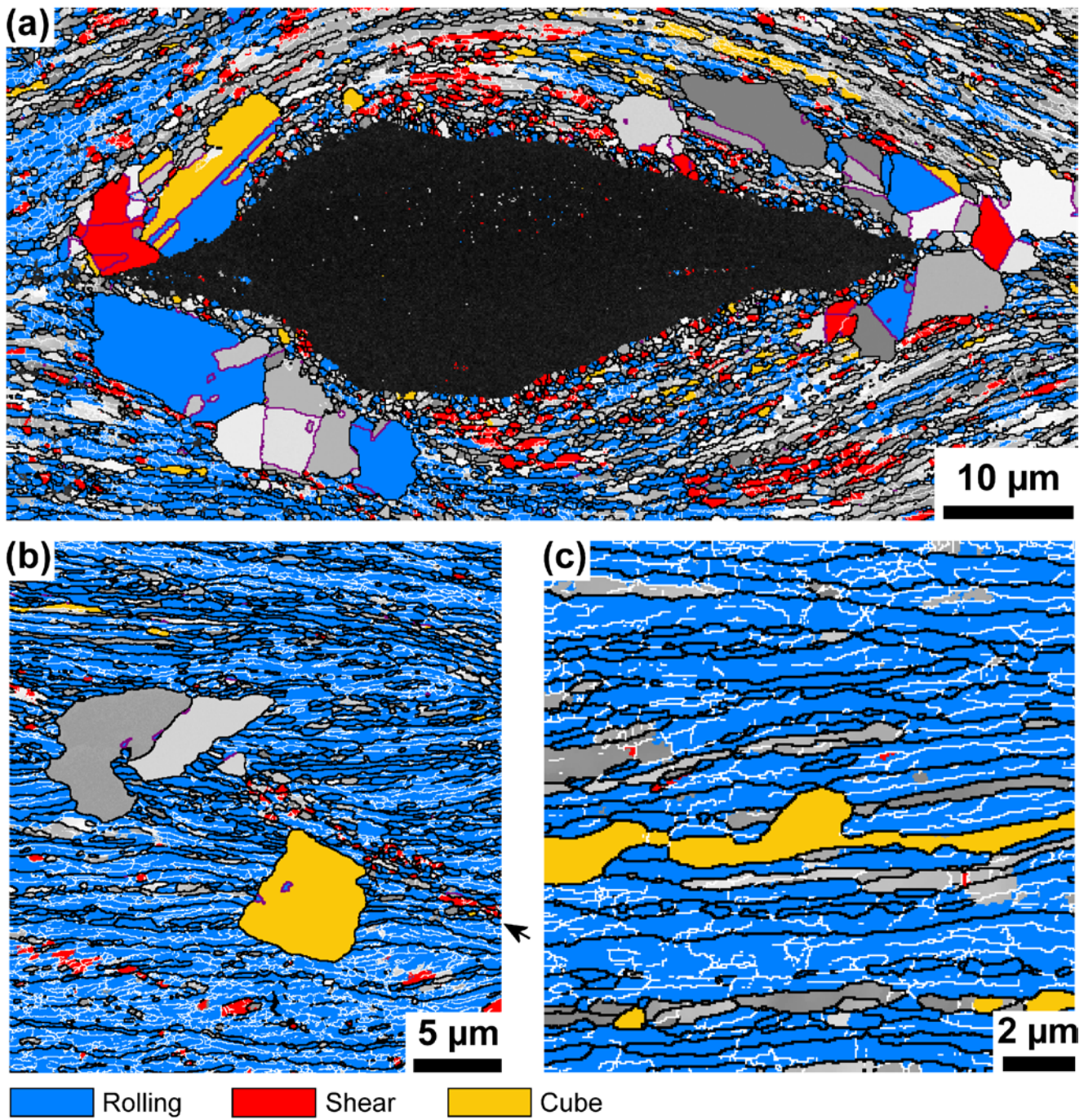


Fig.7

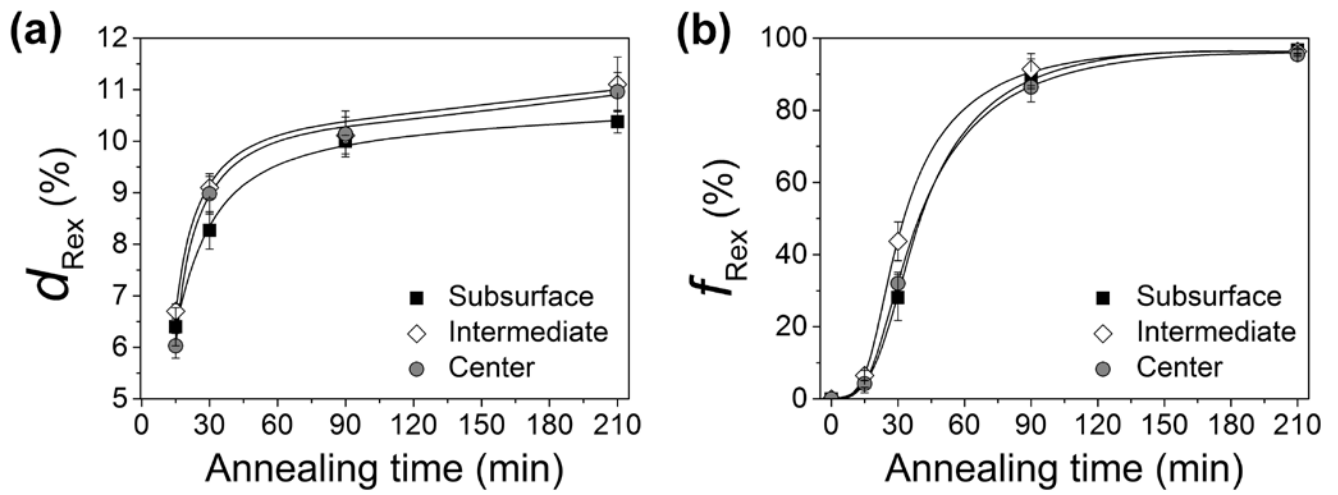


Fig.8

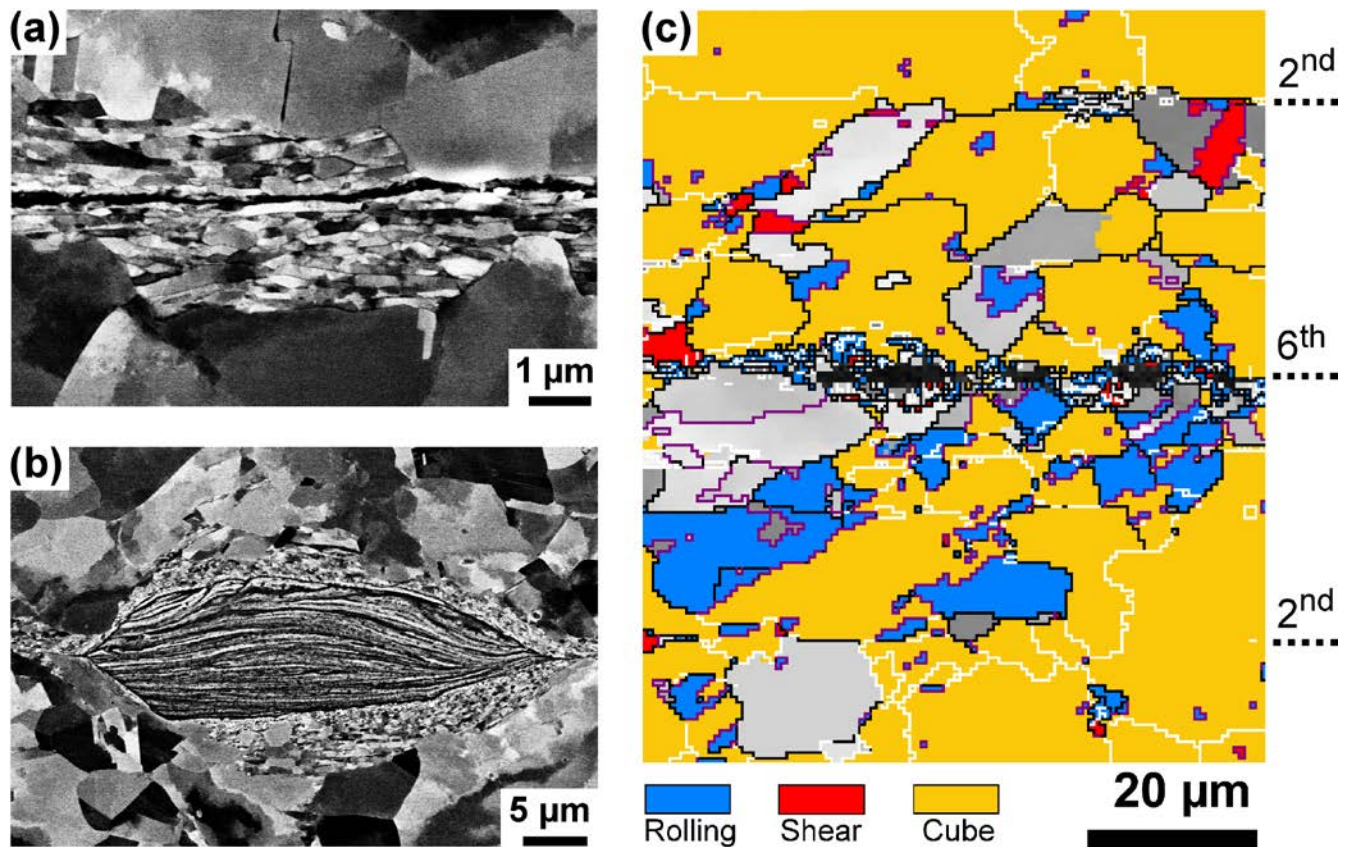


Fig.9

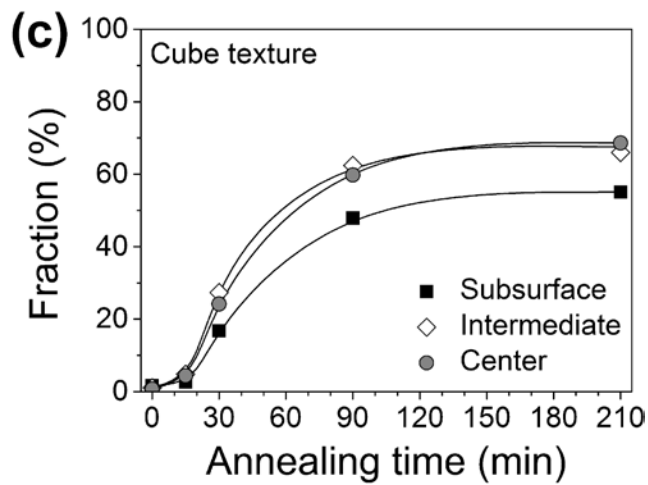
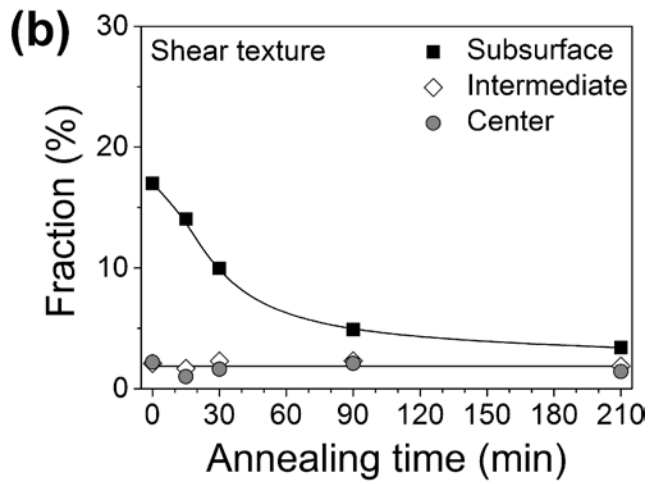
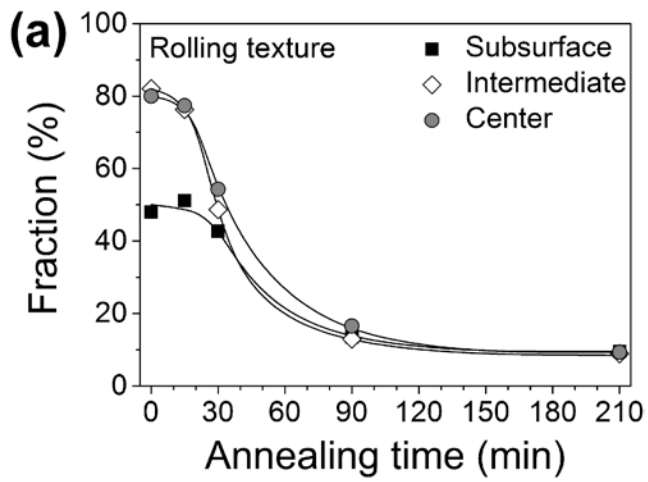


Fig.10

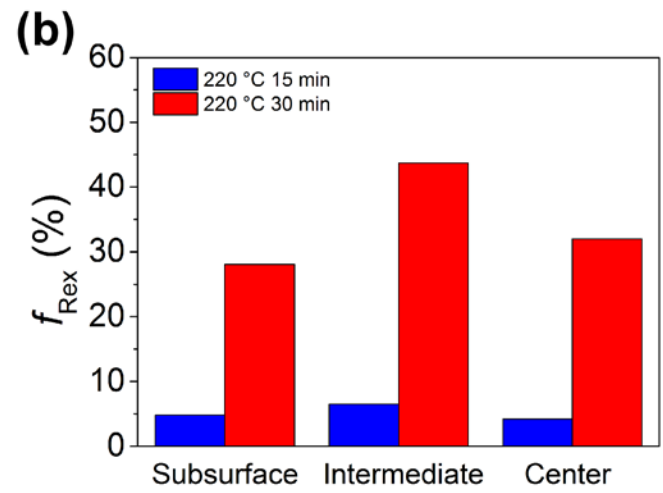
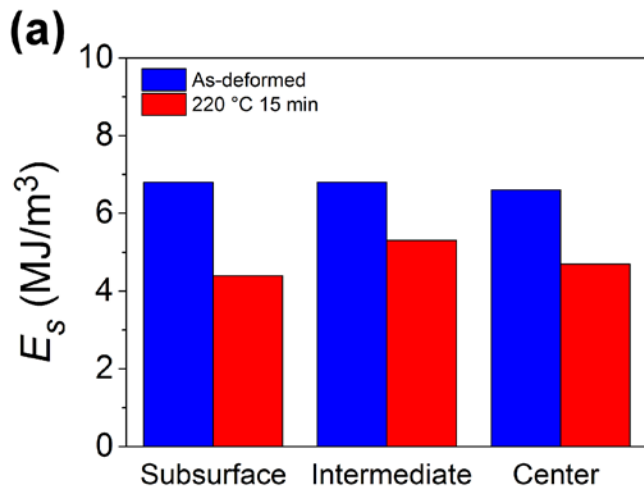


Fig.11

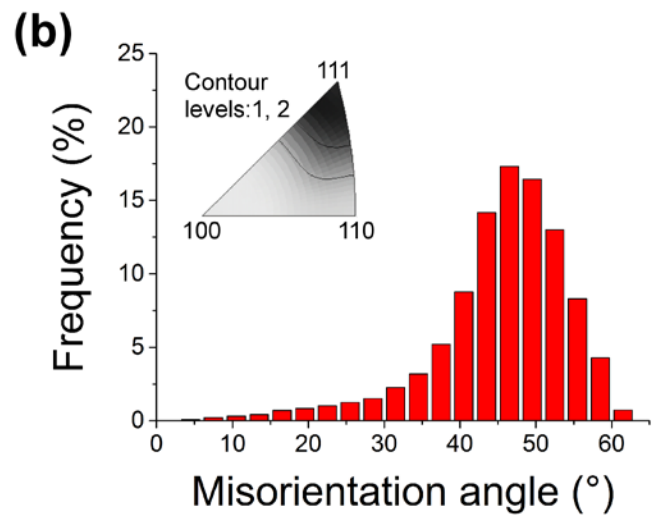
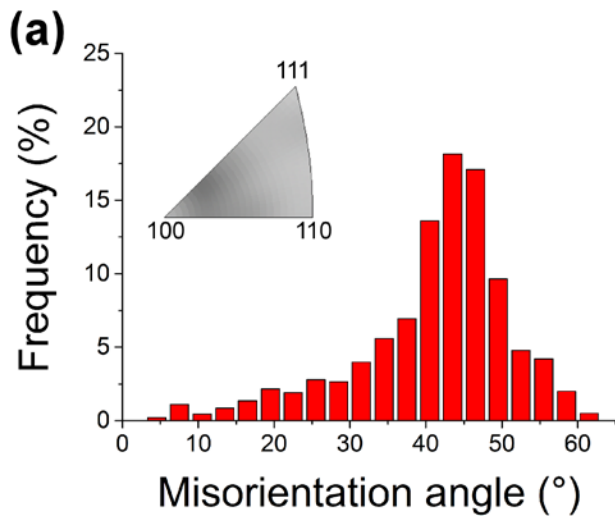


Fig.12

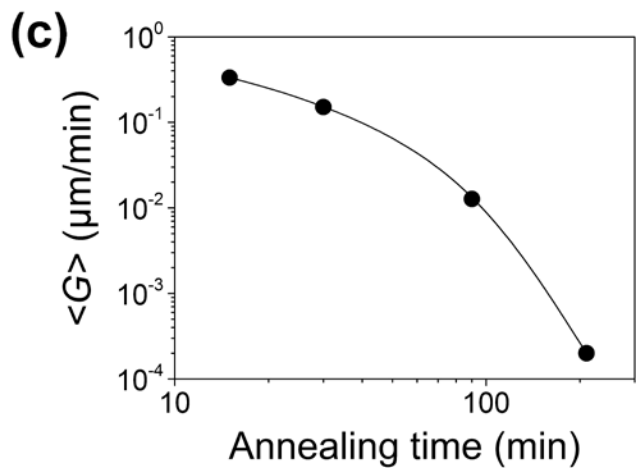
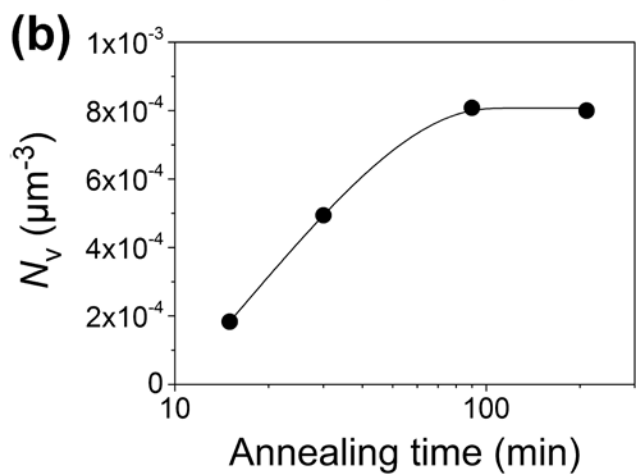
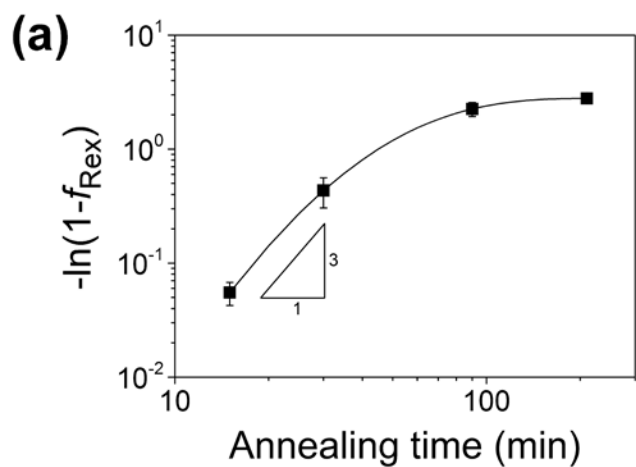


Fig.13